JOURNAL OF THE AMERICAN CHEMICAL SOCIETY

Article

pubs.acs.org/JACS

Mechanistic Studies of the Oxygen Evolution Reaction Mediated by a Nickel–Borate Thin Film Electrocatalyst

D. Kwabena Bediako,[†,‡] Yogesh Surendranath,[†] and Daniel G. Nocera*[,†,‡]

[†]Department of Chemistry, Massachusetts Institute of Technology, 77 Massachusetts Avenue, Cambridge, Massachusetts 02139–4307

[‡]Department of Chemistry and Chemical Biology, Harvard University, 12 Oxford Street, Cambridge, Massachusetts 02138–2902

Supporting Information

ABSTRACT: A critical determinant of solar-driven water splitting efficiency is the kinetic profile of the O_2 evolving catalyst (OEC). We now report the kinetic profiles of water splitting by a self-assembled nickel–borate (NiB_i) OEC. Mechanistic studies of anodized films of NiB_i exhibit the low Tafel slope of 2.3 × $RT/2F$ (30 mV/decade at 25 °C). This Tafel slope together with an inverse third order rate dependence on H^+ activity establishes NiB_i as an ideal catalyst to be used in the construction of photoelectrochemical devices for water splitting. In contrast, nonanodized NiB_i films display significantly poorer activity relative to their anodized congeners that we attribute to a more sluggish electron transfer from the catalyst resting state. Borate is shown to play two ostensibly antagonistic roles in OEC activity: as a promulgator of catalyst activity by enabling proton-coupled electron transfer (PCET) and as an inhibitor in its role as an adsorbate of active sites. By defining the nature of the PCET pre-equilibrium that occurs during turnover, trends in catalyst activity may be completely reversed at intermediate pH as compared to those at pH extremes. These results highlight the critical role of PCET pre-equilibria in catalyst self-assembly and turnover, and accordingly suggest a reassessment in how OEC activities of different catalysts are compared and rationalized.

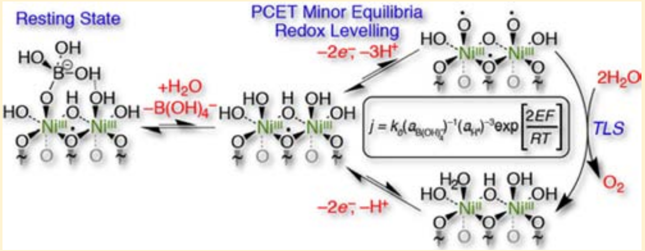

INTRODUCTION

Photodriven water splitting to generate H_2 and O_2 is a promising means of storing solar energy in chemical fuels.[1−5] Viable solar-to-fuels schemes mandate the use of catalysts that can mediate the oxygen evolution reaction (OER) and hydrogen evolution reaction (HER) with minimized overpotentials required to sustain current densities commensurate with the solar flux (ca. 20 mA/cm^2).[4] Of the two half reactions, the OER is more kinetically demanding because it requires a total of four redox equivalents per turnover, and results in the formation of two oxygen–oxygen bonds.[6,7] Accordingly, the majority of the activation overpotential in water splitting usually arises from the OER.[8] Oxygen evolution catalysts (OECs) must therefore be able to accommodate the redox demand of the OER, ideally over a narrow potential range. Such activity profiles (i.e., small current–voltage, Tafel, slopes) are especially important for the integration of catalysts with light harvesting/charge separating materials in a buried-junction configuration.[1,9−12] In a buried-junction semiconductor heterostructure,[11−15] a photovoltage is generated at an internal solid-state junction of a photovoltaic (PV) material that is protected from the electrolyte by an Ohmic coating. Such a configuration is an especially attractive target for direct solar-to-fuels conversion because the catalytic and PV components can be independently optimized, thus permitting the use of a wider variety of semiconductor and catalytic materials.[16] In a buried junction device, the kinetic behavior of the catalysts defines the point of intersection of the electrochemical load of the catalyst with the current density–voltage (j–V) curve of the PV.[14,17] This impedance matching determines the operational current density and voltage, and therefore net solar–to–fuels efficiency (SFE) of the system. The highest SFEs demand that OECs possessing modest exchange current densities and low Tafel slopes be integrated with PVs that have open circuit voltages near the thermodynamic threshold of water splitting.[17] Since the Tafel slope depends on the mechanism of the reaction itself, the development of functionally stable and efficient buried junction systems requires an understanding of the interplay between the kinetics of catalyst formation/decomposition and catalytic turnover.[18] Moreover, catalysts that are stable and operate at intermediate pH regimes are particularly useful because they avoid OER conditions where semiconducting materials are often unstable.

To meet the foregoing requirements, we have elaborated Co–OECs that operate under a range of conditions, including the underexplored intermediate pH regimes.[18−26] The Co–OEC displays a 60 mV/decade Tafel slope and an inverse first order dependence on H^+ activity owing to the presence of a Co^{III}–OH/Co^{IV}–O PCET pre-equilibrium during turnover.[24]

Received: December 27, 2012
Published: January 29, 2013

dx.doi.org/10.1021/ja3126432 | J. Am. Chem. Soc. 2013, 135, 3662−3674

Although this catalyst has been successfully applied to a myriad of semiconducting materials,[13,27−39] and is the foundation on which the artificial leaf has been built,[9] improvements in SFE may be realized with the development of more active catalysts, particularly those with lower Tafel slopes. To this end, we recently reported a nickel−borate (NiB$_i$) system that allows for controlled electrodeposition of OEC films that display high activity at intermediate pH.[25] X-ray absorption spectroscopy reveals changes in the nickel oxidation state and local structure that accompany a drastic improvement (ca. 3 orders of magnitude) in activity upon anodization of NiB$_i$[26] as a result of Tafel slopes of 30 mV/decade (2.3 × RT/2F) in near-neutral pH regimes.[17,26] In line with anodization pretreatment, complementary studies have shown that solution-cast Ni-based and NiFe-based films also furnish low Tafel slopes in alkaline pH regimes.[40] Electrochemical treatment of the crystalline oxide precursors appears to lead to transformation of the films into a nickelate structure[40] that is very similar to that found for NiB$_i$ films in near neutral regimes.[26] Moreover, we have shown that phase changes induced by electrochemical conditioning of conventional crystalline oxides is a crucial factor to consider in OEC development.[41] In light of this emerging trend of increased activity with anodization of Ni−based catalysts, we sought to correlate OEC activity with anodization.

We now report the OER kinetic profile of NiB$_i$ films over a wide pH range (8.5−14) and divulge mechanistic insights into the origin of the considerable activity enhancement that is attendant to anodization. The electrosynthesis of ultrathin OEC films (≤15 monolayers) enables us to avoid internal electronic or ionic transport barriers. Our studies have enabled us to uncover a unique OER mechanism that stands in contrast to frequently invoked OER mechanisms of nickel oxide anodes.[42−50] Furthermore, we find that the apparent specific activity of NiB$_i$ films is significantly greater than that found in CoB$_i$ systems of comparable catalyst loading for pH > 7. However, the same pH-dependent profiles cause CoB$_i$ to supersede NiB$_i$ in activity for pH ≤ 7. By defining the nature of the proton-coupled electron transfer (PCET) pre-equilibrium that occurs during turnover, we find that trends in catalyst activity may be completely reversed at intermediate pH as compared to those at pH extremes. The results presented herein highlight the need for a detailed mechanistic understanding of OER for the construction of direct solar-to-fuels devices that operate at high efficiencies.

EXPERIMENTAL SECTION

1. Materials. Ni(NO$_3$)$_2$·6H$_2$O 99.9985% was used as received from Strem. KOH 88%, KNO$_3$ 99.0−100.5%, and H$_3$BO$_3$ 99.9% were reagent grade and used as received from Macron. NaClO$_4$ hydrate (99.99% metals basis) was used as received from Aldrich. All electrolyte solutions were prepared with type I water (EMD Millipore, 18 MΩ cm resistivity). Fluorine−tin−oxide (FTO) coated glass (TEC-7) was purchased as pre-cut 1 cm × 2.5 cm glass pieces from Hartford Glass. Unless stated otherwise, all experiments used FTO with 7 Ω/sq surface resistivity.

2. Electrochemical Methods. Potentiometric and voltammetric measurements were undertaken with a CH Instruments 760C or 760D bipotentiostat, a BASi Ag/AgCl reference electrode (soaked in saturated KCl), and a Pt-mesh counter electrode. Rotating disk electrode (RDE) measurements were conducted using a Pine Instruments MSR rotator and a 5 mm diameter Pt-disk rotating electrode. All electrochemical experiments were performed at 23 ± 1 °C using a three-electrode compartment cell with a porous glass frit separating the working and auxiliary compartments. Electrode potentials were converted to the NHE scale using $E(\text{NHE}) = E(\text{Ag/AgCl}) + 0.197$ V. Overpotentials were computed using $\eta = E(\text{NHE}) - 0.68$ V at pH 9.2. Unless stated otherwise, the electrolyte comprised 0.5 M potassium borate (KB$_i$), 1.75 M potassium nitrate, pH 9.2 (henceforth referred to as KB$_i$/KNO$_3$ electrolyte).

3. Film Preparation. Catalyst films were prepared via controlled-potential electrolysis of 0.1 M KB$_i$, pH 9.2 electrolyte solutions containing 0.4 mM Ni^{2+}. To minimize precipitation of Ni(OH)$_2$ from these solutions, 25 mL of 0.2 M KB$_i$ was added to 25 mL of 0.8 mM Ni^{2+} solution. The deposition solutions were subsequently filtered through a 0.2 μm syringe filter (Pall) to remove any Ni(OH)$_2$ that formed. The solutions thus prepared remained clear over the course of deposition, which was carried out onto an FTO-coated glass piece. These FTO working electrodes were rinsed with acetone and water prior to use. A ~0.6 cm wide strip of Scotch tape was applied to the FTO coated side such that a 1 cm^2 area was exposed to solution. Unless stated otherwise, deposition by controlled potential electrolysis was carried out on quiescent solutions at 1.15 V without *iR* compensation and with passage of 1 mC cm^{-2}. A typical deposition lasted 70 s. Following deposition, films were rinsed by dipping briefly in 0.1 M KB$_i$, pH 9.2 solution to remove any adventitious Ni^{2+}. Anodized films were subsequently electrochemically treated in 1 M KB$_i$, pH 9.2 electrolyte by passing an anodic current of 3.5 mA cm^{-2} with stirring. A steady potential was obtained after about 30 min of anodization. Unless stated otherwise, films were anodized for 1 h.

4. Potentiostatic Tafel Data Collection. Current−potential data were obtained by conducting controlled potential electrolysis in KB$_i$/KNO$_3$ electrolyte pH 9.2 at a variety of applied potentials (E_{appl}). Prior to film deposition and anodization, the solution resistance of the electrolyte to be used for Tafel data collection was measured using the *iR* test function. The electrolysis solution was exchanged for Ni^{2+}-containing KB$_i$ electrolyte, without disturbing the relative positions of the working and reference electrodes and films were deposited. Following film preparation, the working electrode was rinsed in fresh Ni-free KB$_i$ electrolyte and transferred, without drying, to the same electrolysis bath in which the solution resistance was measured. The electrode was allowed to equilibrate with the electrolyte solution for 5 min while being held at the open circuit potential. The solution was stirred, and steady-state currents were then measured at applied potentials that descended from 1.13 to 1.00 V in 7−20 mV steps. For currents greater than 10 μA cm^{-2}, a steady state was reached at a particular potential in less than 400 s. For currents lower than 10 μA cm^{-2}, longer electrolysis times (15−20 min) were utilized to ensure that steady state had been achieved. The solution resistance measured prior to the data collection was used to correct the Tafel plot for Ohmic potential losses. Tafel data collected in succession using the same electrode exhibited good reproducibility, and Tafel slopes were not dependent on the direction of potential change (Figure S2).

5. Cyclic Voltammetry. CVs of anodized catalyst films were recorded in KB$_i$/KNO$_3$, pH 9.2 electrolyte. After 2 min at open circuit, catalyst films were held at 1.0 V for 60 s, immediately after which CV scans were initiated from 1.0 V. The potential was decreased at a scan rate of 100 mV s^{-1} with stirring, and with correction for Ohmic potential losses (measured prior to film deposition). At a switching potential of 0.2 V, the direction of scan was reversed, and CVs were terminated at 1.1 V.

6. Dependence of Tafel Data on Film Thickness and Calculation of Lower-Limit TOF. Steady-state polarization data were acquired following anodization of films deposited by passage of 1.0, 0.4, and 0.083 mC cm^{-2}. Deposition durations were about 67, 25, and 11 s, respectively. We note that the charge passed cannot be used as a simple measure of the Ni loading because: (1) non-Faradaic double-layer charging currents for short deposition times (and particularly for the thinnest of these films) accounts for a non-trivial proportion of the total charge passed; and (2) oxygen evolution accompanies deposition, and so a fraction of the charge passed is consumed for OER and not solely for film deposition. Thus, in order to evaluate film loadings, CVs of each film were acquired as described in part 5 of this section, and the charge consumed upon film reduction was determined by integration of the cathodic surface wave. Charges of 0.91, 0.53, and 0.21 mC cm^{-2} were obtained from analysis of the CVs.

We have established that the charge passed upon film oxidation or reduction involves the net transfer of 1.6 electrons per nickel center for films of comparable thickness.[26] Thus, the charges correspond to loadings of about 5.9, 3.4, and 1.4 nmol/cm^2 of Ni centers, corresponding to films of approximate thicknesses of 5, 3, and 1.0 nm.

Knowing the amount of nickel on each electrode, and by interpolating Tafel data for each film at η = 400 mV, respective current densities, j, at this overpotential can be converted into turnover frequency per nickel center, given that each turnover requires the removal of four electrons ($j = 4F\nu$, where ν is the turnover velocity of the film per cm^2 and F is the Faraday constant). Dividing ν by the catalyst loading returns the TOF per nickel center. Since the number of active sites is expected to be only a fraction of the number of nickel centers, this calculation returns a lower limit for the TOF of each active site. The calculated lower limit on the TOFs at η = 400 mV in 0.5 M KB_i 1.75 M KNO_3, pH 9.2 are 0.92, 0.51, and 0.49 mol O_2 (mol Ni)$^{-1}$ s^{-1} for films deposited by passage of 1.0, 0.4, and 0.08 mC cm^{-2}, respectively. Similarly, in the case of a 1.0 mC cm^{-2} catalyst film operated in 1 M KOH 1 M KNO_3 pH 13.85 electrolyte, we calculate a lower-limit on the TOF of 1.7 mol O_2 (mol Ni)$^{-1}$ s^{-1} at η = 325 mV.

7. Mass Transport Dependence Studies. To verify that Tafel data were not subject to mass transport limitations, a Pt rotating disk electrode (RDE) was used to collect steady state data. The Pt RDE was polished to a mirror finish with 0.05 μm α-alumina (CH Instruments). Prior to film deposition, the Pt disk was electrolyzed at 1.4 V (vs NHE) in 1 M KB_i, pH 9.2 electrolyte for 30 min to anodize the Pt surface exhaustively as to minimize current arising from platinum oxide formation upon application of a potential step. Following this pretreatment, catalyst films were deposited onto the Pt RDE in an otherwise identical manner to that described above. Tafel data were collected in KB_i/KNO_3 electrolyte with E_{appl} stepped from 1.13 to 1.00 V in 7–20 mV increments. At each potential step, steady-state data were collected at rotation rates (ω) of 2000 and 600 rpm; data were also collected in the absence of disk rotation, but in a well-stirred solution. *iR* corrected Tafel data collected under these three conditions are shown in Figure S1. Background currents arising from the OER at the Pt RDE itself are insignificant compared to currents due to the OER mediated by NiB_i. The excellent agreement among Tafel slopes (28 mV/decade) under these disparate conditions reveals that Tafel data are not limited by mass transport over the current/potential range explored. In addition, these experiments demonstrate that the kinetic profile of the catalyst does not depend on the nature of the underlying substrate.

8. Tafel Data in the Absence of Excess Supporting Electrolyte. Tafel data were acquired as in part 2 of this section, with the exception that electrolytes contained only KB_i and no KNO_3. Tafel data were collected in 0.1, 0.2, 0.5, and 1.0 M KB_i, pH 9.2 electrolyte (Figure S3). Apparent Tafel slopes decrease from 40 to 35 mV/decade as the borate concentration (and ionic strength of the electrolyte) increases.

9. Supporting Electrolyte Effect. The surface of a 0.2 cm^2 FTO-coated glass electrode was exposed by application a 1 cm wide piece of scotch tape to isolate a 2.0 mm ×1.0 cm strip. The solution resistances of six electrolytes, each containing 0.1 M KB_i at pH 9.2, with varying concentrations of KNO_3 from 0 to 2 M were measured using the *iR* test function. Without disturbing the relative positions of the working and reference electrodes, a 1.0 mC cm^{-2} catalyst film was deposited and anodized. Following anodization, the catalyst film was operated in each solution at a fixed current density of 0.4 mA cm^{-2}. In this galvanostatic experiment, the potential required to sustain this current density was recorded after at least 300 s had elapsed. Potential values were then corrected for *iR* drop using the measured solution resistances. Prior to operation in each electrolyte, the catalyst film was briefly rinsed in fresh electrolyte of identical composition, to avoid cross-contamination. As shown in Figure S4, KNO_3 concentrations ≥1 M are sufficient to eliminate any diffuse double layer effects and attendant complications arising from elevated local concentrations of borate anions.

10. Open Circuit Decay Transients. NiB_i films were prepared as described in part 3 of this section. Following deposition, the films were immersed in KB_i/KNO_3 pH 9.2 electrolyte and held at 1.1 V (vs NHE) for 10 s, after which E_{appl} was removed. This short duration was sufficient for the current to plateau without the onset of anodization. A second potentiostat, which was connected in parallel, was used to measure the voltage across the working and reference electrodes throughout the potential bias and for 2 min subsequent to the removal of E_{appl} (open circuit). The sampling interval was 5 ms. The open circuit potential (OCP) was plotted as a function of time (see Figure 2). The electrode was then rinsed in water and anodized in 1 M KB_i pH 9.2 electrolyte. Following anodization, films were immersed in KB_i/KNO_3 pH 9.2 electrolyte, and the open circuit decay experiment was repeated, this time with a sampling interval of 2.5 ms. The open circuit potential was plotted as a function of time (see Figure 2). These transients were fit to eq 1 to extract the Tafel slopes for OER for anodized and nonanodized films. The OCP transients were also converted into Tafel plots (Figure 2 inset) using eq 2.

11. Borate Dependence Studies. To determine the reaction order in borate, solutions were prepared with B_i concentrations in the range 0.63–6.3 mM. An appropriate amount of KNO_3 was added to ensure an ionic strength of 2 M. The solution resistance of each electrolyte was recorded without disturbing the relative positions of the working and reference electrodes, and then a 1.0 mC cm^{-2} catalyst film was deposited onto a Pt RDE. Following anodization, the catalyst film was operated at 1.05 V in each solution at ω = 2500, 1600, 900, and 625 rpm. At each rotation rate, the current was allowed to reach its steady-state value before proceeding to the next rate. Prior to operation in each electrolyte, the catalyst was rinsed in fresh electrolyte of identical composition to avoid cross-contamination. The experiment was then repeated at 1.04 and 1.06 V. Ohmic losses due to solution resistance accounted for <1 mV, and they were therefore neglected. Appreciable changes in current values with ω were observed for electrolytes of low buffer strength ($[B_i]$ < 40 mM), implying that the reaction was not purely activation controlled. As such, Koutecký–Levich (K–L) plots (i^{-1} as a function of $\omega^{-1/2}$) were constructed to allow for extraction of activation-controlled currents by linear extrapolation to the limit of an infinitely high rotation rate (Figure S5 shows a representative plot). Log j was plotted as a function of log $[B_i]$ (see Figure 3) over the $[B_i]$ range 0.63 M–40 mM. In electrolytes of very low buffer strength ($[B_i]$ < 40 mM), a slope of ca. zero is observed.

12. pH Dependence Studies in B_i Electrolyte. A 0.2 cm^2 (1 cm × 2 mm) area of an FTO-coated glass electrode was isolated with scotch tape and a 1 mC cm^{-2} catalyst film was deposited. The electrode was operated at a current of 2 μA (equivalent to 10 μA cm^{-2}) in 100 mM KB_i 2 M KNO_3, pH 8.5 electrolyte. The steady state electrode potential (measured after operation for ≥2 min at each pH) was recorded as the pH of the solution was raised up to pH 12.0 in increments of about 0.1 pH units using μL aliquots of 10% KOH solution. Ohmic potential losses amounted to <0.1 mV, and they were ignored. Additionally, at these very low current densities, no local pH gradients arise even when the pH is adjusted outside of the ideal B_i buffering regime. The steady-state electrode potential was plotted as a function of pH (see Figure 4).

A 1.0 mC cm^{-2} catalyst film was prepared onto a Pt RDE. Tafel data were collected in electrolytes with B_i concentrations equal to 0.601, 0.200, 0.110, 0.101, and 0.100 M at pH 8.5, 9.2, 10.2, 11.2, and 12.0, respectively, to ensure that each electrolyte contained ~0.1 M borate anion, considering the pK_a of 9.2 for B_i buffer. Sufficient KNO_3 was added to each solution to yield a concentration of 0.9 M, and therefore to maintain an ionic strength of 1 M. In each solution, steady state data were collected without *iR* compensation at 2500, 1600, 900, and 625 rpm, and where necessary, K–L analysis was used to extract activation–controlled current values. Although the measured current, and for that matter the *iR* drop, varied with rotation rate, the difference in these Ohmic losses due to solution resistance between different rotation rates at the same applied potential was negligible (<1 mV). The product of the previously measured solution resistance and the average current value over the rotation rate range analyzed was subtracted from the applied potential to yield the *iR*-corrected potential. The upper and lower limits for applied potentials were chosen such that current densities would fall between 3.5 mA cm^{-2} and 10 μA cm^{-2}. Data were recorded at potential intervals of 10 mV to yield Tafel slopes (Figure 5a). Tafel plots were interpolated at 2.5, 0.25, and 0.025 mA cm^{-2} to furnish the potential dependence on pH at constant current density (Figure 5b).

13. pK_a Titrations. A 1.0 mC cm^{-2} catalyst film was prepared onto an FTO-coated glass electrode (0.2 cm^2), and operated at a current of 2 μA (equivalent to 10 μA cm^{-2}) in 100 mM $\mathrm{KB_i}$ 2 M $\mathrm{KNO_3}$, pH 11.3 electrolyte. The steady-state electrode potential was recorded using a Hg/HgO (1 *m* NaOH) reference electrode as the pH of the solution was raised in increments of 0.2−0.25 pH units up to pH 12, with μL aliquots of 50% KOH solution. The experiment was continued in separate electrolytes of identical composition (100 mM $\mathrm{KB_i}$ 2 M $\mathrm{KNO_3}$) whose pH had been previously adjusted to pH 12.25, 12.5, 12.8, and 13.15, respectively. Ohmic potential losses amounted to <0.1 mV in each electrolyte and could be safely ignored. The measured potentials (vs Hg/HgO) were converted to the NHE scale using E(NHE) = E(Hg/HgO, 1 *m* NaOH) + 0.108.[51] The corresponding overpotentials were calculated by subtracting the thermodynamic potential for the OER at each pH from the E(NHE) values. The steady state electrode overpotential was plotted as a function of pH at 10 μA cm^{-2} (see Figure 6).

14. Tafel Data in $\mathrm{B_i}$-Free Electrolyte, pH 12.9, 13.8. A 1.0 mC cm^{-2} catalyst film was deposited onto a Pt RDE, and Tafel data were acquired in 0.1 M KOH 1.9 M $\mathrm{KNO_3}$ and 1.0 M KOH 1.0 M $\mathrm{KNO_3}$ solutions (pH 12.9 and 13.8, respectively). For these solutions, no mass transport limitations were encountered over the accessible overpotential range (η = 220−330 mV), and activation-controlled steady state Tafel data were acquired at a single rotation rate of 2000 rpm (Figure 6, inset).

15. Tafel Data in $\mathrm{B_i}$-Free Electrolyte, pH 8.5. A 1.0 mC cm^{-2} catalyst film was deposited onto a Pt RDE as described above. The activation-controlled steady state current density was measured with *iR* compensation as a function of applied potential by K−L analysis (see Figure S6 for a representative example) at 20 mV intervals in 1.0 M $\mathrm{NaClO_4}$, pH 8.50 electrolyte. There were 1−5 μL aliquots of 1 M NaOH added periodically to ensure minimal drift (±0.01 pH units) in bulk pH over the course of the experiment. Three consecutive runs were acquired, and the Tafel data were averaged (Figure 7). The activities of films in $\mathrm{B_i}$ electrolyte (0.5 M $\mathrm{KB_i}$ 1.75 M $\mathrm{KNO_3}$, pH 9.2 electrolyte) after operation in 1 M $\mathrm{NaClO_4}$ pH 8.5 are compared with Tafel data acquired using a fresh catalyst film in Figure S7. Since the activity of a catalyst film after operation in $\mathrm{B_i}$-free electrolyte is comparable to that of a fresh film, the possibility of film corrosion causing the Tafel behavior displayed in Figure 7 is excluded.

16. Deposition and Tafel Plots of $\mathrm{CoB_i}$ Films. $\mathrm{CoB_i}$ catalyst films were prepared via controlled-potential electrolysis of 0.1 M $\mathrm{KB_i}$, pH 9.2 electrolyte solutions containing 0.5 mM $\mathrm{Co^{2+}}$. Depositions were carried out using an FTO-coated glass piece as the working electrode. These FTO-coated glass electrodes were rinsed with acetone and water prior to use in all experiments and a ∼0.6 cm wide strip of Scotch tape was applied to the FTO coated side such that a 1 cm^2 area was exposed to solution. Deposition by controlled potential electrolysis was carried out on quiescent solutions at 0.9 V (vs NHE) without *iR* compensation and with passage of 0.6 mC cm^{-2} (equivalent to 6 nmol cm^{-2} Co). A typical deposition lasted 12 s.

Current−potential data were obtained for this 0.6 mC cm^{-2} $\mathrm{CoB_i}$ film by conducting controlled potential electrolysis in $\mathrm{KB_i/KNO_3}$ pH 9.2 electrolyte at a variety of applied potentials. Prior to film deposition, the solution resistance of the electrolyte to be used for collection of Tafel data was measured using the *iR* test function. The electrolysis solution was exchanged for $\mathrm{Co^{2+}}$-containing $\mathrm{KB_i}$ electrolyte, without disturbing the relative positions of the working and reference electrodes. The film was prepared by controlled-potential electrolysis. Following film preparation, the working electrode was rinsed in fresh Co-free $\mathrm{KB_i}$ electrolyte and transferred, without drying, to the same electrolysis bath in which the solution resistance was measured. The electrode was allowed to equilibrate with the electrolysis solution for 5 min while being held at the open circuit potential. The solution was stirred, and steady-state currents were then measured at applied potentials that descended from 1.13 to 1.00 V in 10 mV steps. At each potential, 400 to 600 s were allowed for the film to reach steady state. The solution resistance measured prior to the data collection was used to correct the Tafel plot for Ohmic potential losses (Figure 9a).

RESULTS

Catalyst films were prepared by controlled potential electrolysis of 100 mM $\mathrm{KB(OH)_4/H_3BO_3}$ ($\mathrm{B_i}$) electrolyte, pH 9.2 containing 0.4 mM $\mathrm{Ni^{2+}}$ at an applied potential of 1.15 V (vs NHE) without stirring. Unless otherwise noted, a total charge of 1.0 mC cm^{-2} was passed during deposition over a period of 60−80 s using fluorine−tin−oxide (FTO) coated glass slides as substrate. Following deposition, films were preconditioned with an anodization protocol that involved passage of 3.5 mA cm^{-2} for 1−2 h in stirred solutions of 1.0 M $\mathrm{B_i}$ electrolyte, pH 9.2.

1. Tafel Slope Determination. The steady-state current density (j) for oxygen evolution from anodized films was evaluated as a function of the overpotential (η) in stirred Ni-free solutions of 0.5 M $\mathrm{B_i}$ pH 9.2 electrolyte (Figure 1). To avoid diffuse double layer effects,[52] a high ionic strength was maintained with 1.75 M $\mathrm{KNO_3}$ supporting electrolyte. The applied voltage (E_{appl}) was varied in 7−20 mV increments in the region of water oxidation and maintained until j attained a steady-state value. Compensation of E_{appl} for Ohmic potential losses yielded the corrected potential (E), which was then converted to η by subtraction of the thermodynamic potential for water oxidation ($E°$) under the experimental conditions. Steady-state polarization data were acquired following anodization of films deposited by passage of 1.0, 0.40, and 0.083 mC cm^{-2}.

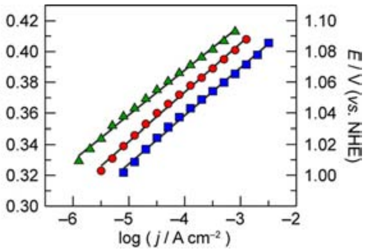

Figure 1. Tafel plots, $E = (E_{\mathrm{appl}} - iR)$, $\eta = (E - E°)$, for anodized catalyst films deposited onto FTO by passage of 1.0 (blue ■), 0.40 (red ●), and 0.083 (green ▲) mC cm^{-2} and operated in 0.5 M $\mathrm{KB_i}$ 1.75 M $\mathrm{KNO_3}$ pH 9.2 electrolyte. Tafel slopes are 31, 32, and 29 mV/decade, respectively.

The amount of charge passed in oxidation or reduction of $\mathrm{NiB_i}$ films involves a net transfer of ca. 1.6 electrons per nickel center.[26] With this knowledge, the charge consumed upon reduction of films by cyclic voltammatery permits a reliable estimation of the number of nickel centers in catalyst films (see subheading 6 of the Experimental Section) and thickness of the films.[26] Film thicknesses of approximately 5, 3, and 1 nm correspond to 15, 9, and 3 monolayers' worth of catalyst, respectively. Although the overall activity of these catalyst films at a specified overpotential increases with thickness, plots of η (or E) as a function of log j (Tafel plots) display similar slopes, b, of 30 mV/decade (2.3 × $RT/2F$), irrespective of loading. These Tafel slopes are indicative of a two-electron transfer in minor equilibrium prior to a chemical turnover-limiting step (TLS), resulting in a transfer coefficient, α ($\alpha = 2.3RT/bF$) of 2.[45,53] Tafel plots of films deposited onto a Pt rotating disk electrode (RDE) are identical irrespective of the rotation rates, ω of 2000 or 600 rpm, or whether stirring is the sole source of convection (Figure S1). These observations confirm that the Tafel slope is representative of activation-controlled OER over the potential range explored. Tafel slopes are also reproducible for sequential runs, and do not depend on the direction of potential change (Figure S2), indicating that the films are not significantly altered over the course of data collection.

Although only a fraction of the nickel centers may be involved in catalysis, a lower-limit value for the oxygen evolution turnover frequency ($\mathrm{TOF_{min}}$) of $\mathrm{NiB_i}$ catalyst films at a specified overpotential can be estimated by determining the rate of turnover per nickel center in the film at that overpotential. At η = 400 mV in 0.5 M $\mathrm{B_i}$ pH 9.2 electrolyte, a $\mathrm{TOF_{min}}$ was determined to be 0.9, 0.5, and 0.5 mol $\mathrm{O_2}$ (mol Ni)$^{-1}$ s^{-1} for films prepared by passage of 1.0, 0.40, and 0.083 mC cm^{-2}, respectively (see subheading 6 of the Experimental Section).

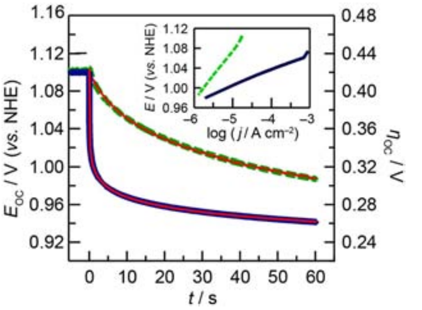

Figure 2. Open circuit potential, E_{OC}, and overpotential, $\eta_{OC} = (E_{OC} - E°)$, transients for nonanodized (green ---) and anodized (dark blue —) 1.0 mC cm^{-2} $\mathrm{NiB_i}$ films immediately following a 10 s bias at 1.1 V in 0.5 M $\mathrm{KB_i}$ 1.75 M $\mathrm{KNO_3}$ pH 9.2 electrolyte. The red lines represent fits to eq 1. Tafel slopes are 100 before anodization and 33 mV/decade after anodization. The inset shows the corresponding Tafel plots determined from the E_{OC} transients by calculating log j at each time point using eq 2.

Tafel slopes were also extracted from open circuit potential (E_{OC}) decay transients, following the interruption of a potential pulse. Catalyst films were poised at 1.1 V in 0.5 M $\mathrm{B_i}$ pH 9.2 electrolyte for 5 s. Upon switching to open circuit, the decay in E_{OC} was monitored as a function of time, t (Figure 2). The decrease in E_{OC} arises due to the discharge of the capacitance of the electrode, through the Faradaic resistance, mediated by the catalyst film (i.e., Ni centers in the film are reduced by water via the OER). Thus, the characteristics of the overpotential of the electrode at open circuit ($\eta_{OC} = E_{OC} - E°$) versus time depend on the mechanism of $\mathrm{O_2}$ evolution and therefore the Tafel slope, b[43,54,55]

$$\eta_{OC} = a - b\log(t + \tau) \tag{1}$$

with $a = b\log(bC/j_0)$ and $\tau = 10^{(-\eta'/b)}bC/j_0$. C is the capacitance of the electrode, j_0 is the exchange current density, and η' is the initial overpotential at t = 0. This open-circuit decay method assumes that any change in C during the experiment is negligible.

E_{OC}−t curves recorded for anodized and non−anodized films are shown in Figure 2.

Owing to their considerably higher catalytic activity, the E_{OC} of anodized films decreases by almost 100 mV within the first 0.1 s after the potential is interrupted. In contrast, over the same duration a minimal decrease (<10 mV) is observed in E_{OC} for nonanodized films. Fitting the decay trace of an anodized film to eq 1 yields a Tafel slope of 33 mV/decade, which is in excellent agreement with the steady-state Tafel plot measurements of Figure 1. In contrast, a much higher Tafel slope of 100 mV/decade is extracted from the open circuit decay trace of nonanodized films. These transients permit the construction of Tafel plots of anodized and nonanodized films by recognizing that the instantaneous OER current density across the catalyst−electrolyte interface (log j_t) can be expressed as a function of the time elapsed during the OCP decay, t[54]

$$\log j_t = \log j_{t=0} - \log(1 + t/\tau) \tag{2}$$

where log $j_{t=0}$ is the initial current density before open circuit conditions. The resulting Tafel plots (Figure 2 inset) illustrate a significant difference in the activity of anodized versus nonanodized films. We note that the Tafel plot of the anodized film is concordant with that obtained by steady state polarization measurements of Figure 1.

2. Determination of Reaction Order in $\mathrm{B_i}$. The dependence of reaction rate on buffer strength was interrogated by controlled potential electrolysis of anodized catalyst films at 1.04, 1.05, and 1.06 V in Ni-free electrolyte, pH 9.2 with varying $\mathrm{B_i}$ concentrations $[\mathrm{B_i}]$ from 630 to 6.3 mM (Figure 3).

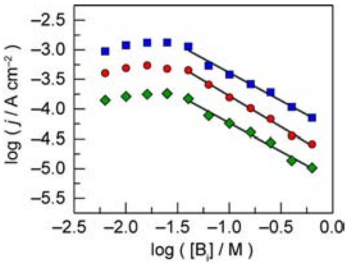

Figure 3. $\mathrm{B_i}$ concentration dependence of steady state catalytic current density at constant potential (E = 1.04 V (green ◆), 1.05 V (red ●), 1.06 V (blue ■)) for an anodized catalyst film deposited onto a Pt RDE by passage of 1.0 mC cm^{-2} and operated in $\mathrm{B_i}$ electrolyte, pH 9.2. Sufficient $\mathrm{KNO_3}$ was added to maintain a constant total ionic strength of 2 M in all electrolytes. Koutecký−Levich analysis was used to extract activation-controlled current densities in weakly buffered electrolyte, where the measured current was dependent on rotation rate. The experimental reaction orders (slopes of the red linear fits) in $\mathrm{B_i}$ are (from top to bottom) −0.95, −1.04, and −0.95.

Sufficient $\mathrm{KNO_3}$ was added to each solution to preserve a constant high ionic strength of 2 M. Diffuse double layer effects,[52] which lead to spuriously elevated Tafel slopes and distorted reaction orders (Figure S3), can be eliminated by operating at constant ionic strength as well as maintaining a low concentration of buffering species relative to an inert supporting electrolyte (Figure S4).[56] Catalyst films were deposited onto a Pt RDE that had been pretreated to render any current due to Pt oxide formation negligible (see subheading 7 of the Experimental Section). For each electrolyte examined, the RDE was operated until a steady-state current value was attained at various ω. In cases where the $[\mathrm{B_i}]$ was less than 100 mM, the observed currents were subject to mass transport limitations, as evidenced by the dependence of i on ω. In these instances, Koutecký−Levich (K−L) plots of i^{-1} as a function of $\omega^{-1/2}$ were constructed (Figure S5) to extract the activation-controlled current values by linear extrapolation to the limit of infinitely high rotation rates ($\omega^{-1/2} \rightarrow 0$).[57,58] In all cases, Ohmic potential losses amounted to less than 1 mV, and therefore, they were neglected. Figure 3 shows the logarithm of the activation−controlled current density plotted as a function of log[B_i]. For [B_i] ≥ 40 mM, the slope of the plot establishes an inverse first order dependence of current density on B_i activity. In electrolytes of very low buffer strength ([B_i] < 40 mM), film activity deviates from this reaction order, and an ostensibly zeroth order regime is observed.

3. Determination of Reaction Order in H^+ Activity. Given the explicit reaction order in B_i, any measurements of reaction rate dependence on pH will inevitably alter the activity of boric acid, borate anion, or both. To evaluate the reaction order in H^+ activity, anodized films were deposited onto a Pt RDE, and steady-state data were collected as a function of pH. Initially, a galvanostatic titration at 10 μA cm^{-2} in an electrolyte with a constant $[B_i]_{total}$ = 100 mM was undertaken in the presence of 2 M KNO_3. The titration was commenced at pH 8.5, and the potential required to sustain constant current density was measured as the pH of the solution was raised incrementally. At low current density, no local pH gradients arise, even when the pH is adjusted outside of the ideal B_i buffering regime. Additionally, Ohmic potential losses were less than 0.5 mV, and they can be neglected. The plot of potential as a function of pH (Figure 4) shows two limiting slopes of −64 mV/pH unit and −96 mV/pH unit for pH ranges 8.5−9.8 and 10−12, respectively. The bifurcation observed at pH 10 indicates that either (1) there is a change in mechanism (such as a change in Tafel slope) at pH 10 or (2) there exists an inverse first order dependence of reaction rate on only borate anion (B_i^-), and not on boric acid, $B(OH)_3$, such that as the pH is increased from 8.5−10, the corresponding exponential increase in the concentration of B_i^- serves to skew the true dependence on H^+ activity. In this case, the intrinsic proton order is observed for pH > 10 where [B_i^-] reaches saturation.

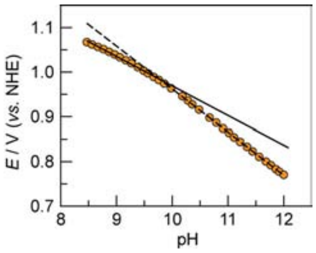

Figure 4. pH dependence of steady-state electrode potential at constant current density (j_{anodic} = 10 μA cm^{-2}) for an anodized 1.0 mC cm^{-2} catalyst film on FTO operated in 0.1 M B_i 2 M KNO_3 electrolyte. Slopes equal −64 (—) and −96 (---) mV/pH unit.

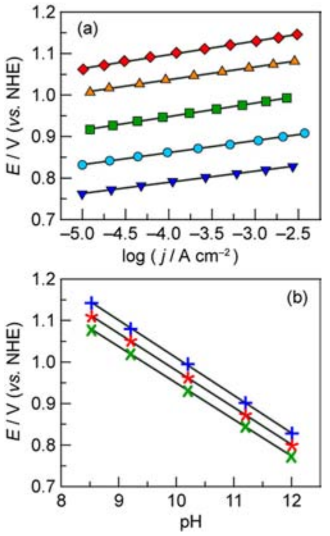

Figure 5. (a) Tafel plots, $E = (E_{appl} - iR)$, for anodized NiB$_i$ catalyst films deposited on a Pt rotating disk electrode by passing 1.0 mC cm^{-2}, and operated in 0.60 M B_i pH 8.5 (red ◆), 0.20 M B_i pH 9.2 (orange ▲), 0.11 M B_i pH 10.2 (green ■), 0.10 M B_i pH 11.2 (light blue ●), and 0.10 M B_i pH 12.0 (dark blue ▼). Each electrolyte contained an additional 0.9 M KNO_3 as supporting electrolyte to maintain an ionic strength of about 1 M. Koutecký−Levich plots were constructed to extract activation-controlled current densities where necessary. (b) Interpolation of Tafel plots at 2.5 mA cm^{-2} (blue +), 0.25 mA cm^{-2} (red ∗), and 0.025 mA cm^{-2} (green ×). Slopes are −90, −89, and −88 mV/pH unit, respectively.

A separate experiment was conducted to distinguish between scenarios 1 and 2. Films were deposited onto a Pt RDE, and Tafel data were collected using B_i solutions at pH 8.5, 9.2, 10.2, 11.2, and 12.0 (Figure 5a). In each electrolyte, the total buffer concentration [B_i] was varied such that the concentration of borate anion [B_i^-] was maintained at 100 mM; 0.9 M KNO_3 was added to each solution to preserve a constant ionic strength of 1 M. Where necessary, the activation-controlled current densities were obtained from K−L analysis. There is no mechanistic change over the pH range explored; all Tafel slopes lie between 28 and 32 mV/decade. This suggests that scenario 2 is at the root of the change observed for pH > 10. Interpolation of each Tafel plot at 2.5, 0.25, and 0.025 mA cm^{-2} yields the potential dependence on pH (Figure 5b). The single observed slope $(\partial E/\partial \mathrm{pH})_j$ = −90 mV/pH over the pH range 8.5−12.0 is a convolution of the pH dependence of the current density $(\partial \log j/\partial \mathrm{pH})_E$ and the potential dependence of the current density $(\partial E/\partial \log j)_{\mathrm{pH}}$. That is[59]

$$\left(\frac{\partial E}{\partial \mathrm{pH}}\right)_j = -\left(\frac{\partial \log j}{\partial \mathrm{pH}}\right)_E \left(\frac{\partial E}{\partial \log j}\right)_{\mathrm{pH}} \tag{3}$$

Substituting $(\partial E/\partial \mathrm{pH})_j$ = −90 mV/pH (from Figure 5b) and $(\partial E/\partial \log j)_{\mathrm{pH}}$ = 30 mV/decade (the Tafel slope) into eq 3 gives $(\partial \log j/\partial \mathrm{pH})_E$ = +3. The reaction order in H^+ activity $(\partial \log j/\partial \log a_{H+})_E$ may thus be determined as

$$\left(\frac{\partial \log j}{\partial \log a_{H^+}}\right)_E = -\left(\frac{\partial \log j}{\partial \mathrm{pH}}\right)_E \tag{4}$$

which yields a reaction order in proton activity a_H^+ of −3. We therefore deduce that the reaction rate is zeroth order in boric acid activity, inverse first order in borate anion activity for [B_i^-] in excess of 20 mM, and inverse third order in proton activity between pH 8.5 and pH 12.

A galvanostatic titration in 100 mM B_i from pH 11 to 13 was used to investigate a change in the pH dependence under alkaline conditions, which might be expected to arise when the pH is elevated beyond the pK_a of an active site species. As shown in Figure 6, a plateau in the plot of η versus pH is observed at pH ∼ 12.2. However, since Tafel data acquired in 0.1 and 1.0 M KOH (Figure 6 inset and Figure S8) continue to exhibit slopes close to 29 mV/decade, the mechanistic change that results in this plateau in the η versus pH plot does not arise from changes in Tafel slope. Instead, this behavior must arise exclusively from changes in the H^+ reaction order.

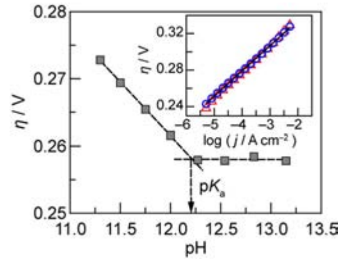

Figure 6. Plot of the pH dependence of steady-state electrode overpotential (gray ■), at constant current density (j_{anodic} = 10 > μA cm^{-2}) for an anodized 1.0 mC cm^{-2} catalyst film deposited onto FTO and operated in 0.1 M B_i 2 M KNO_3 electrolyte. The change in slope at pH 12.2 is consistent with the elevation of the bulk pH above the pK_a of an active site moiety. The inset shows Tafel plots, $\eta = (E - iR - E°)$, for anodized catalyst films deposited onto a Pt RDE by passage of 1.0 mC cm^{-2} and operated at 2000 rpm in 0.1 M KOH 1.9 M KNO_3 pH 12.9 (blue ○) and 1.0 M KOH 1.0 M KNO_3 pH 13.8 (red △) electrolyte. Tafel slopes are 28 and 30 mV/decade, respectively.

According to Figure 6, for pH > 12.2 there is no dependence of the current density on pH at constant overpotential. This parameter, $(\partial \log j/\partial \mathrm{pH})_\eta$, is related to the pH dependence of the current density at constant potential, $(\partial \log j/\partial \mathrm{pH})_E$, through the transfer coefficient, α ($\alpha = 2.3RT/bF$, where b is the Tafel slope):[59]

$$\left(\frac{\partial \log j}{\partial \mathrm{pH}}\right)_E = \left(\frac{\partial \log j}{\partial \mathrm{pH}}\right)_\eta + \alpha \qquad (5)$$

Both Tafel slopes are close to 29 mV/decade, and therefore, $\alpha = 2.3RT/0.029F = 2$. Substituting $(\partial \log j/\partial \mathrm{pH})_\eta = 0$ and $\alpha = 2$ into eq 5, we find $(\partial \log j/\partial \mathrm{pH})_E = 2$. According to eq 4, this results in a reaction order in H^+ activity of −2. Therefore, the reaction order in H^+ activity transitions from a value of −3 over the range pH 8.5 to 12 (Figure 5a,b) to −2 at pH ≥ 12.2 (Figure 6). These results indicate that one of the three kinetically relevant protic centers of NiB_i active sites possesses a pK_a of 12.2. In strongly alkaline electrolytes, this species is deprotonated in the resting state of the catalyst and ceases to contribute to the electrochemical rate law.

4. Tafel Data in B_i-Free Electrolyte. To explore OER kinetics in the absence of a weak base, steady state polarization data were collected in 1 M $NaClO_4$ pH 8.5 solution. Films were deposited onto a Pt RDE by passage of 1.0 mC cm^{-2} and anodized in B_i buffered solutions. Tafel data were obtained in $NaClO_4$ electrolyte by extrapolation of K−L plots at each potential considered (Figure S6) in order to eliminate mass transport limitations through the bulk electrolyte. Over the course of the experiment, small aliquots (1−5 μL) of 1 M NaOH were added periodically to preserve the bulk pH at 8.50(1). Tafel data are the average of three runs. The resulting Tafel plot displays a greatly elevated slope compared to Tafel data acquired in B_i electrolyte, pH 8.5 (Figure 7). The kinetic profile of catalyst films in B_i buffered media following operation in B_i-free electrolyte was comparable to the activity of a freshly prepared film (Figure S7), indicating that the Tafel behavior obtained in the absence of B_i cannot be attributed to the corrosion of catalyst films in buffer−free electrolyte.

■ DISCUSSION

1. Steady-State Tafel Data. Tafel behavior describing the effect of potential, E, or overpotential, η, on steady-state current density, along with experimentally determined reaction orders, forms the basis of the mechanistic analysis of oxygen evolution by NiB_i catalyst films. Steady-state current densities are proportional to the activation-controlled velocity of the OER if the reaction is not subject to mass-transport limitations. This requirement is true of the electrokinetic studies described herein, since in well-buffered electrolytes Tafel data collected using an RDE is identical irrespective of rotation rate or whether stirring was the sole means of mass transport with the electrode stationary (Figure S1), resulting in Tafel slopes, b (where $b = \partial E \partial \log j)_{\mathrm{pH}}$, of 28 mV/decade in each case. In cases where mass transport limitations were encountered (poorly buffered media, or electrolytes completely lacking a weak base electrolyte), Koutecký−Levich analysis was employed to extract activation-controlled current densities. Furthermore, the Tafel plots are the same for sequential runs and independent of the direction of potential change during data acquisition (Figure S2), verifying that catalyst films are not altered appreciably over the course of experiments. Precise control of catalyst film thickness was accomplished by managing the total charge passed during deposition. Although the resultant film thicknesses ranged from 1 to 5 nm (equivalent to 3−15 monolayers of catalyst), Tafel plots collected for each film gave similar slopes, close to 30 mV/decade (Figure 1). Since activated transport through the film can impose additional potential barriers to electronic/ionic conductivity,[60−62] consistent slopes over a range of film thicknesses (particularly at almost monolayer coverage) demonstrate the absence of non-Ohmic potential losses between the potential applied at the electrode and that experienced by active sites. In our initial report,[25] we explored considerably thicker films (>1 μm thick), and higher Tafel slopes were observed. However, the data reported here is for ultrathin (1−5 nm) films. Thus, these results are consistent with sluggish charge or mass transport through the mesoporous films leading to an inflation of the Tafel slope at high catalyst loadings. For anodized catalyst films, Tafel plots (Figure 1) yield 30 mV/decade slopes that are consistent with a mechanism involving a chemical turnover-limiting step (TLS) that follows a two-electron pre-equilibrium. The reciprocal of the Tafel slope in dimensionless form is known as the transfer coefficient, $\alpha = 2.3RT/bF = 2$ for b = 29.5 mV/decade at 25 °C.[59] Although the Tafel slopes are independent of film thickness, the apparent exchange current

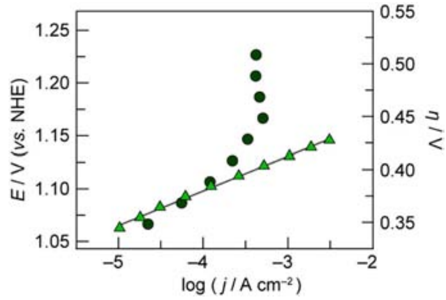

Figure 7. Tafel plots, $E = (E_{\mathrm{appl}} - iR)$, $\eta = (E - E°)$, for anodized catalyst films deposited onto a Pt RDE by passage of 1.0 mC cm^{-2} and operated in 1 M $NaClO_4$ pH 8.5 electrolyte (●). Koutecký−Levich analysis of steady state current densities at various rotation rates was used to eliminate mass transport limitations through solution. The data shown is the average of three consecutive runs. A Tafel plot of an identical catalyst film in 0.6 M KB_i 0.9 M KNO_3 pH 8.5 (0.1 M B_i^-, total ionic strength = 1 M) electrolyte (green ▲), displaying a 32 mV/decade Tafel slope (—), is shown for comparison.

densities and hence the overall activity of films does increase with loading. This would be expected to occur, as anodes with thicker catalyst layers should possess more active sites per unit geometric area in these porous films. Lower-limit TOFs of 0.9 mol O_2 (mol Ni)$^{-1}$ s^{-1} are observed at η = 400 V in pH 9.2 electrolyte and 1.7 mol O_2 (mol Ni)$^{-1}$ s^{-1} at η = 325 mV in 1 M KOH. Lower-limit TOF for these catalysts may be calculated at any η by recognizing that the TOF decreases by an order of magnitude per 30 mV increment. Thus, these catalyst films rival the most active OER anodes reported to date.[40]

2. OER of Nonanodized NiB$_i$. Monitoring the decay in open circuit potential after interrupting an applied potential bias offers a complementary means of determining the Tafel slope of an electrokinetic reaction.[43,54,55] This method is the most appropriate means of extracting electrokinetic information on the OER at the less catalytically active nonanodized films, since polarization of the electrode for an extended period of time leads to anodization.[26] The higher activity of anodized films is immediately evident in the very rapid decay at early times due to more efficient O_2 evolution as compared to the less catalytically active nonanodized films (Figure 2). Indeed, since the Tafel slope for anodized films is found to be 33 mV/decade (in agreement with Figure 1), the corresponding OCP-decay transient indicates that the surface concentration of catalytic intermediates in anodized NiB$_i$ decreases by over 3 orders of magnitude in the first 100 ms after the potential is removed. In contrast, the Tafel slope of nonanodized films is considerably higher, approaching 100 mV/decade. Tafel slopes of 120 (±20) mV/decade are expected for mechanisms involving a turnover-limiting electron transfer (ET) from the resting state:[45,59]

$$A \xrightarrow{\text{TLS}} B + e^- \tag{6}$$

The turnover velocity for such a reaction will be given by

$$v = k_{ET}\theta_A \tag{7}$$

where k_{ET} is the rate constant for the turnover limiting electron transfer, and θ_A is the surface coverage of the resting state species, A:[63]

$$\frac{\Gamma_A}{\Gamma_{max}} \tag{8}$$

Γ_A is the surface concentration of active sites that exist in state A (expressed in mol/cm^2), and Γ_{max} is the total surface concentration of active sites. It is important to note that Γ_{max} need not equal the surface concentration of solvent-exposed metal centers, or even the concentration of electroactive Ni centers, since the number of active sites may actually represent a very small proportion of these centers. Under Langmuir conditions, since A is the resting state, θ_A may be assumed to be a constant equal to 1.[63] The rate constant k_{ET} is given by

$$k_{ET} = k^0_{ET} \exp\left(\frac{\beta\eta F}{RT}\right) \tag{9}$$

The parameter k^0_{ET} is the ET rate constant at η = 0, and β is the symmetry factor for the microscopic (irreversible) ET step, which determines the amount of the total driving force due to η (i.e., $\Delta G = -\eta F$), that causes a decrease in the activation energy barrier (i.e., $\Delta(\Delta G^\ddagger) = -\beta\eta F$).[53] Thus, the electrochemical rate law for a reaction that proceeds by eq 6 will be

$$j = 4Fk^0_{ET} \exp\left(\frac{\beta\eta F}{RT}\right) \tag{10}$$

This will lead to a Tafel slope ($\partial\eta/\partial\log j$) of 2.3 × $RT/\beta F$. β is usually close to 0.5 (±0.1),[53] resulting in a Tafel slope of around 120 mV/decade at 298 K. Importantly, in this case, the symmetry factor, β, and the transfer coefficient for the overall OER, α, are numerically identical, since the kinetics of the overall multielectron reaction are governed entirely by the microscopic rate-limiting ET step.[53] In cases where one or more electron transfers exist in equilibrium, β and α are distinct.

It is unclear whether the suppression of the Tafel slope of nonanodized films from 120 mV/decade to 100 mV/decade arises due to the existence of a marginally altered β-value of 0.6, or is a result of the unavoidable partial anodization of the film during deposition.[26] However, the existence of a turnover-limiting electron transfer in nonanodized films is reasonable. The resting state nickel valency in nonanodized films is predominantly +3, and the local coordination environment of Ni centers in such films would be expected to exhibit a Jahn–Teller (J–T) distortion that is expected for low-spin d^7 ions.[26] Thus, the first oxidation process during turnover may be expected to be kinetically sluggish, as it would incur a large reorganizational energy penalty associated with a low-spin d^7 → d^6 transformation. We conclude therefore that a higher reorganizational energy associated with Ni^{3+} oxidation may contribute to a slower electron transfer and thus to very low catalytic activity of nonanodized NiB$_i$ films.

3. OER of Anodized NiB$_i$. XAS shows that anodization of NiB$_i$ films leads to a gradual phase change (involving changes in both local structure and resting state nickel valency) that eliminates the J–T distortion present in nonanodized films.[26] In the absence of structural distortion in local geometry, the oxidation of Ni centers in anodized films should be more facile. Indeed, the 30 mV/decade Tafel slope obtained by steady-state Tafel plots (Figure 1) and open-circuit decay transients (Figure 2) indicates that the turnover-limiting step is chemical in nature and does not involve ET.

Before evaluating the dependence of activity on pH and therefore the existence of proton-transfer (PT) equilibria prior to the TLS, it was necessary to establish the dependence of reaction rate on buffer strength, since any [B$_i$] dependence would have to be accommodated during pH changes. The resulting inverse first order dependence of current density on [B$_i$] over almost 1.5 decades (Figure 3) is consistent with the reversible dissociation of a B$_i$ species from an active site over this range in buffer strength. Boric acid and borate species are known to adsorb to oxide surfaces in aqueous media by coordination to the metal centers.[64−67] The −1.0 reaction order in borate (Figure 3) establishes that the ligation of the buffer species is governed by the Langmuir isotherm with a high surface coverage of the adsorbate.[63] Accordingly, the B$_i$-free active sites necessarily exist in minor equilibrium with a B$_i$-bound resting state. We note that our data cannot distinguish adsorption of polyborate species[68−70] as opposed to $B(OH)_4^-$. Decreasing the concentration of B$_i$ in the electrolyte gives rise to an increase in activation-controlled current density until a point where there appears to be no dependence of reaction velocity on B$_i$ (<40 mM B$_i$).

While demonstrating an association between buffering species and active sites, B$_i$ dependence studies alone could not distinguish which B$_i$ species (boric acid, borate anion (B$_i^-$), or both) must dissociate from active sites during turnover for oxygen to be evolved. The pH dependence of the steady-state electrode potential at a constant high ionic strength changes from about −60 mV/pH over the B_i buffering range to about −90 mV/pH at B_i^- saturation (Figure 4). In contrast, Tafel data collected between pH 8.5 and pH 12 at a constant concentration of borate anion exhibit Tafel slopes of approximately 30 mV/decade (Figure 5a). The pH dependence of the steady-state electrode potential was determined to be about −90 mV/pH by interpolating the Tafel plots at constant current density (Figure 5b). These results identify that the observed desorption step involves the liberation of one borate anion into bulk electrolyte per active site, and confirms a three-proton equilibrium prior to the TLS. Were both species to be liberated from active sites, the activity of boric acid *and* borate in solution should appreciably modulate OER kinetics on NiB_i films, and an experiment in which the total B_i (boric acid + borate) concentration is held constant as the pH is varied (Figure 4) should yield a single slope and the genuine reaction order in H^+ activity. However, if the desorption equilibrium applies to only one species of the conjugate pair, the pH dependence of reaction rate will inevitably be convoluted with the reaction order in that species unless the total B_i concentration is adjusted to maintain a constant activity in the coordinated species alone (Figure 5a,b), or the pH regime is such that B_i speciation does not change appreciably with pH (pH > 10 in Figure 4).

Electrokinetic data should be acquired in an excess of supporting electrolyte. If not, the potential dependence of anion migration and the effects on local pH and specific adsorption of borate will skew Tafel data and lead to slopes that are dependent on B_i concentration, and apparent fractional reaction orders (Figure S3). These effects are eliminated by maintaining a constant, high ionic strength ($I \geq 1$ M) using an inert supporting electrolyte such as KNO_3, which when present at an appreciable concentration serves to reduce the transference number of borate anion (the fraction of the total ionic current that is carried by borate anions) (Figure S4).

Taken together, the results of Figures 1−5 reveal the electrochemical rate law for oxygen evolution in moderate to high borate ion concentrations (20−300 mM) at anodized NiB_i films to be

$$j = k_0(a_{\mathrm{Bi^-}})^{-1}(a_{\mathrm{H^+}})^{-3}\exp\left(\frac{2EF}{RT}\right) \tag{11}$$

where k_0 is proportional to the exchange current density and independent of potential. This rate expression contains the inverse first order dependence on borate activity as shown in Figure 3, the inverse third order dependence on proton activity (Figures 4 and 5), as well as the factor of 2 (transfer coefficient) in the exponential term in the applied potential, E. At constant borate activity and pH and $T = 25$ °C, the partial derivative of E with respect to log j ($\partial E/\partial \log j$) yields a Tafel slope of 30 mV/decade, consistent with Figures 1 and 5a.

The experimental rate law in eq 11 is consistent with the mechanistic sequence

$$\mathrm{A} \rightleftharpoons \mathrm{B} + \mathrm{B_i^-} + 2e^- + 3\mathrm{H}^+ \qquad K_1 \tag{12}$$

$$\mathrm{B} \rightarrow \mathrm{C} \qquad k_2 \tag{13}$$

which involves reversible borate dissociation from the resting state, and a two-electron, three-proton equilibrium followed by a chemical TLS. K_1 is the equilibrium constant at $E = 0$, and k_2 is the rate constant for the chemical TLS. Equation 12 may indeed proceed in a number of discrete steps; however, these would all exist as quasiequilibria, and such a sequence is kinetically indistinguishable from a single step. In addition, there may be any number of distinct chemical equilibrium steps prior to the TLS, but these cannot be resolved kinetically.

According to eq 13, the steady-state velocity of oxygen evolution can be expressed as[53]

$$v = k_2\theta_{\mathrm{B}} \tag{14}$$

θ_B represents the partial surface coverage of intermediate B. θ_B can be defined in terms of the surface coverage of the resting state A (θ_A) as follows[53]

$$\theta_{\mathrm{B}} = K_1\theta_{\mathrm{A}}(a_{\mathrm{Bi^-}})^{-1}(a_{\mathrm{H^+}})^{-3}\exp\left(\frac{2EF}{RT}\right) \tag{15}$$

which involves the application of the Nernst equation to eq 12. Substituting for θ_B in eq 14 gives

$$v = k_2K_1\theta_{\mathrm{A}}(a_{\mathrm{Bi^-}})^{-1}(a_{\mathrm{H^+}})^{-3}\exp\left(\frac{2EF}{RT}\right) \tag{16}$$

If Langmuir conditions are assumed, the surface coverage of the resting state is high, and θ_A would not be expected to change appreciably over the potential range, and may be considered a potential-independent constant equal to 1.[63] In this case, eq 16 approximates the experimental rate law (eq 11) with

$$k_0 = 4Fk_2K_1\theta_{\mathrm{A}} \tag{17}$$

In situ XAS studies of anodized NiB_i films[26] show that there is no systematic shift in the nickel K-edge position with E_{appl} over the potential range used for Tafel data acquisition. This result is consistent with the assumption that the speciation of the resting state, A, is invariant over the potential range explored and therefore permits θ_A to be taken as a constant (eq 17 above). XANES[26,71] spectra and coulometric[26] studies also established that the average oxidation state of Ni in anodized catalyst films was +3.6 to +3.8, thereby indicating a substantial amount of formal Ni^{IV} valency in the catalyst resting state.[26] In fact, there appears to be even more formal +4 valency in NiB_i compared to Co−OEC.[22,23] Computational studies of Ni^{IV}-containing extended solid nickelates have demonstrated significant covalency in Ni−O bonding, and extensive delocalization of hole-density onto oxygen centers upon oxidation of the parent Ni^{III} compounds.[72−74] In addition, EPR studies of a tetracobalt cubane model compound possessing one formally Co^{IV} center as a molecular model of our cobalt-based catalyst revealed a radical distributed almost equally over all Co and O ions, effectively leading to a formal oxidation number of $[Co_4^{+3.125}O_4]$.[75] Thus, it is reasonable to expect that this Ni^{IV} valency in the catalyst resting state is distributed extensively over multiple Ni and O centers in the nickel−oxido clusters that form the ordered domains.

Figure 5 is effectively a Pourbaix diagram of the catalyst active sites, indicating that one of the protic species possesses a pK_a of about 12.2. At the pH regimes considered in this study, a $Ni^{III/IV}$—OH_2 resting state is unlikely, given the Pourbaix diagram for nickel.[76] In addition, the point of zero charge (pH_z) for nickel oxides, which defines the average of the pK_a values of surface-bound water (M−OH_2) and surface-bound hydroxyl (M−OH) groups,[77] has been found to be about 8 and 9.75 for $Ni(OH)_2$ and NiO, respectively.[78−80] Thus, we can anticipate the pK_a of a $Ni^{III/IV}$−OH_2 intermediate would be less than 8.

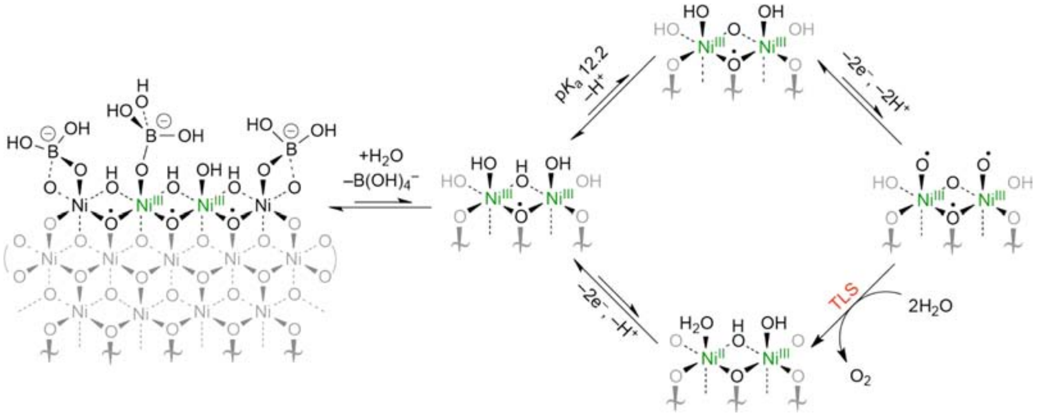

Figure 8. Proposed pathway for O_2 evolution by NiB_i in B_i ($[B(OH)_4^-] > 20$ mM) electrolyte, pH 8.5−14. The reversible dissociation of borate anion and an overall two-electron, three-proton equilibrium followed by a rate limiting chemical step is consistent with the experimental electrochemical rate law. A μ-OH site possessing a pK_a of 12.2 is fully deprotonated in the resting state under highly alkaline conditions. Oxidation state assignments are approximate; oxidizing equivalents are likely extracted from orbitals with predominantly O 2p character, particularly for the pre-TLS intermediate.

The moiety possessing a pK_a of 12.2 can therefore be more reasonably rationalized as a terminal or bridging Ni−OH. Under highly alkaline conditions (specifically pH > 12.2), this species is deprotonated in the resting state resulting in an overall two-electron, two-proton PCET transformation prior to a chemical turnover-limiting step. This gives rise to a 30 mV/decade Tafel slope and −60 mV/pH unit shift of E (Figures 6 and 7). Previous EPR studies[75] have pointed to the importance of proton loss in PCET steps for generating localized reactive intermediates. In the Co−OECs and Ni−OECs, the ensuing change in ligand field strength upon deprotonation could localize the unpaired spin density on specific centers leading to their subsequent reactivity toward O−O bond formation. This concept is validated by computational studies of cobalt oxido clusters as Co−OEC models.[81] Hence, while the resting state valency would be delocalized over the entire cluster, the catalytic intermediates are likely to possess spin density that is more localized due to proton loss.

A mechanistic scheme for oxygen evolution in B_i-buffered electrolyte that is consistent with the interfacial properties of the oxidic surface as well as the electrokinetic data presented herein is shown in Figure 8. For convenience, eq 12 has been described as a sequence of several steps in equilibrium. We assign the two-electron minor equilibrium step to the double oxidation of a dinickel active site, which proceeds with the overall deprotonation of a bridging and two terminal hydroxyl groups. These PCET processes are proposed to lead to a highly oxidized intermediate that may be tentatively described as $[Ni_2^{IV/V}]$ or $[Ni_2^{+4.6}]$. Since this intermediate exists in minor equilibrium at a very low surface coverage, its formal potential must lie well above the potential supplied at the electrode. Nevertheless, this formal $[Ni_2^{IV/V}]$ designation is likely not an accurate description of the true electronic structure of the intermediate; we expect that the electron-transfer pre-equilibria arise from orbitals with predominant O 2p contributions, resulting in oxyl radical character. The loss of three protons must contribute significantly to the accessibility of such highly oxidized intermediates by virtue of the PCET redox-potential leveling effect.[82−84] One hydroxyl group was found to possess a pK_a of 12.2, and hence its corresponding deprotonation step must occur prior to the remaining two-electron, two-proton PCET transformations. Since the turnover-limiting step is chemical in nature and unlikely to involve proton transfer to the electrolyte, we find it reasonable to propose that this step involves O−O bond formation and/or Ni−O bond scission. Computational studies on our Co-based system suggests that direct coupling of two terminal $Co^{IV}(O)$ groups to form an O−O bond is thermodynamically favorable and proceeds with a low kinetic barrier,[81] signifying that it may in fact be the breaking of the metal−oxygen bond that is the turnover-limiting step in these late transition metal oxide catalysts. Spectroscopic studies as well as extensive synthetic and computational modeling will be employed to shed light on the electronic structure of catalytic intermediates and the details of the turnover-limiting process. Further electrochemical studies, particularly on molecular models, are also needed to shed light on the details of the coupled multiproton, multielectron sequences.

4. OER in B_i-Free Electrolyte. Certainly, one important role of B_i is to preserve the local and bulk pH during O_2 evolution. However, the inverse first order dependence of reaction velocity on borate anion activity in eq 15 implicates a deleterious role of borate on OER kinetics. Despite this ostensibly "inhibitory" effect, the crucial importance of borate to the kinetics of water oxidation on NiB_i films is evident in Tafel plots acquired in B_i-free electrolyte (Figure 7). In the absence of B_i, very high Tafel slopes are observed and high current densities cannot be achieved. Since Koutecký−Levich analysis was used to eliminate effects associated with solution mass transport (Figure S6), and the bulk pH was preserved by constant addition of aqueous NaOH, the elevated Tafel slope in B_i-free electrolyte cannot be attributed to pH gradients at the film−solution interface. In addition, following operation in B_i-free electrolyte, films display no loss in activity in B_i-electrolyte (Figure S7), excluding the possibility of catalyst corrosion over the period of polarization in B_i-free electrolyte. The observed Tafel behavior may result from the transition to a turnover-limiting chemical step from the resting state; the absence of any preceding electrochemical steps results in a potential-independent kinetic profile, and therefore an extremely high ("infinite") Tafel slope. We observed a similar result for phosphate-free electrolytes of Co-based catalyst films.[24] These preliminary electrokinetic data suggest that proton transfer processes may become turnover-limiting in the absence of a

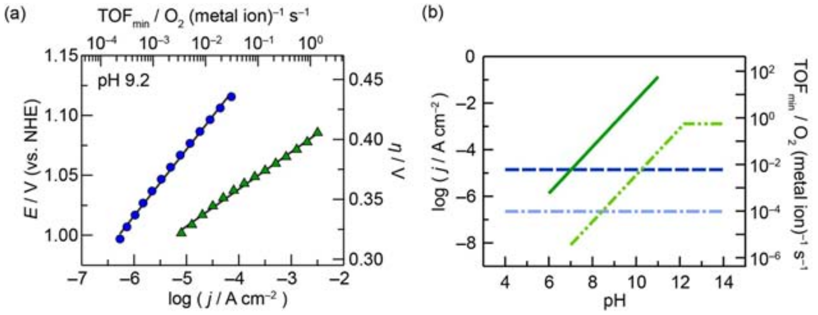

Figure 9. Comparison of ultrathin CoB$_i$ and NiB$_i$ OEC films with identical catalyst loadings of 6 nmol metal ions/cm^2. (a) Tafel plots of CoB$_i$ (blue ●) and NiB$_i$ (green ▲) in 0.5 M KB$_i$ 1.75 M KNO$_3$ pH 9.2 electrolyte. Tafel slopes equal 55 and 31 mV/decade, respectively. (b) Schematic of the pH dependence of the current density and lower-limit turnover frequency of CoB$_i$ at a constant overpotential of 400 mV (dark blue ---) and 300 mV (light blue —·—) compared to that of NiB$_i$ at 400 mV (dark green —) and 300 mV (light green —··—) overpotential. Curves were calculated using the appropriate experimentally determined electrochemical rate laws. Ni-based films display a much higher *apparent* specific activity (since the true number of active sites cannot be known) than Co-based films above pH 8. However, due to their disparate electrochemical rate laws, a crossover is expected to occur around neutral pH, at which point Co-based films would yield higher activity anodes. The precise pH at which crossover occurs depends on the overpotential applied due to the different Tafel slopes.

good proton acceptor, at low hydroxide ion concentrations. Additional studies are ongoing to shed more light on the details of OER under such conditions, but these results underscore the critical importance of borate to facilitating proton transfers, thereby expediting the PCET sequences necessary for rapid O$_2$ evolution.

5. Differences in Mechanism and Activity of Co−OECs and Ni−OECs. Differences in activity between oxido Co−OECs and Ni−OECs are governed to a large extent by the characteristics of the PCET pre-equilibrium. A two-electron oxidation is required before the chemical turnover-limiting step in anodized NiB$_i$ OEC films (30 mV/decade Tafel slope), whereas turnover at Co−OEC films involves a one-electron pre-equilibrium (60 mV/decade Tafel slope). We propose that this difference arises because O−O bond formation in both systems proceeds by radical coupling of two active site oxygen centers.[81] In Co−OEC, this oxygen-centered unpaired spin density arises upon generation of somewhat localized, low-spin formally d^5 Co^{4+} centers.[22,75,81]

Realization of a similar electronic structure would require more substantial oxidation for a nickel catalyst than for a cobalt-based system. As such, it would be expected to lead to a lower exchange current density, but also a lower Tafel slope, provided the ET steps remain kinetically facile. This is indeed what is observed when one compares Co−OEC with NiB$_i$ at comparable catalyst loadings at pH 9.2 (Figure 9a). Additionally, the more extensive oxidation would also demand greater accompanying H$^+$ loss, leading to disparate pH dependences. Because of the differences in pH dependence for the two catalysts, NiB$_i$ increasingly outperforms Co−OEC as the pH is elevated (Figure 9b). However, at neutral pH and slightly acidic conditions, Co−OEC surpasses NiB$_i$ in activity. The majority of studies on the OER have been conducted in highly alkaline media,[85−87] and these have led to useful trends in correlating specific thermodynamic parameters (such as M−O bond strengths, enthalpies of formation of the metal(III) hydroxide compound, and adsorption enthalpies of proposed intermediates) with catalytic activity, resulting in the general consensus that, for first row transition metal oxides, OER activity increases in the order MnO$_x$ < FeO$_x$ < CoO$_x$ < NiO$_x$.[45,62,88−90] However, as evident from Figure 9b, activity trends in concentrated base may not hold in intermediate pH electrolytes because of disparate PCET pre-equilibria involved in the mechanism of the OER at different catalysts.

■ CONCLUSION

Electrodeposited ultrathin anodized NiB$_i$ catalyst films exhibit a Tafel slope of 30 mV/decade in well-buffered electrolytes between pH 8.5 and 14. Electrokinetic studies demonstrate that oxygen evolution in B$_i$-buffered electrolyte entails the reversible dissociation of borate anion from the resting state and a two-electron, three-proton equilibrium followed by a chemical turnover-limiting step. Under highly alkaline conditions, a change in reaction order in proton activity is observed that is attributed to the full deprotonation of a protic center with a pK_a of 12.2. On the basis of previous in situ XAS, a mixed valence Ni$^{III/IV}$ resting state is invoked, although radical character on oxygen ions in this resting state as well as the subsequent catalytic intermediate states is anticipated. These studies highlight the contradicting roles of borate as both an inhibiting adsorbate and a proton acceptor for PCET at intermediate pH. The much lower catalytic activity of nonanodized films may appear to arise, in part, from a large reorganizational energy arising from a Jahn−Teller distorted Ni^{III} resting state found in nonanodized films, thus resulting in a rate-limiting electron transfer. The low Tafel slope of anodized NiB$_i$ films makes this catalyst ideal for integration with buried-junction semiconductors.

■ ASSOCIATED CONTENT

Ⓢ Supporting Information

Additional Tafel plots and representative K−L plots. This material is available free of charge via the Internet at http://pubs.acs.org.

■ AUTHOR INFORMATION

Corresponding Author

nocera@fas.harvard.edu

Notes

The authors declare no competing financial interest.

■ ACKNOWLEDGMENTS

D.K.B. gratefully acknowledges the MIT Energy Initiative for a predoctoral fellowship. Y.S. gratefully acknowledges the National Science Foundation for a predoctoral fellowship. This research was supported jointly by the DOE Solar Photochemistry and Catalysis programs, U.S. DOE Grant DE-FG02-13ER16377.

■ REFERENCES

(1) Cook, T. R.; Dogutan, D. K.; Reece, S. Y.; Surendranath, Y.; Teets, T. S.; Nocera, D. G. *Chem. Rev.* **2010**, *110*, 6474−6502.
(2) Nocera, D. G. *Inorg. Chem.* **2009**, *48*, 10001−10017.
(3) Barber, J. *Chem. Soc. Rev.* **2009**, *38*, 185.
(4) Lewis, N. S.; Nocera, D. G. *Proc. Natl. Acad. Sci. U.S.A.* **2006**, *103*, 15729−15735.
(5) Alstrum-Acevedo, J. H.; Brennaman, K. L.; Meyer, T. J. *Inorg. Chem.* **2005**, *44*, 6802−6827.
(6) Eisenberg, R.; Gray, H. B. *Inorg. Chem.* **2008**, *47*, 1697−1699.
(7) Betley, T. A.; Wu, Q.; Van Voorhis, T.; Nocera, D. G. *Inorg. Chem.* **2008**, *47*, 1849−1861.
(8) Surendranath, Y.; Nocera, D. G. *Prog. Inorg. Chem.* **2011**, *57*, 505−560.
(9) Nocera, D. G. *Acc. Chem. Res.* **2012**, *45*, 767−776.
(10) Walter, M. G.; Warren, E. L.; McKone, J. R.; Boettcher, S. W.; Mi, Q.; Santori, E. A.; Lewis, N. S. *Chem. Rev.* **2010**, *110*, 6446−6473.
(11) Khaselev, O.; Turner, J. A. *Science* **1998**, *280*, 425−427.
(12) Rocheleau, R. E.; Miller, E. L.; Misra, A. *Energy Fuel* **1998**, *12*, 3−10.
(13) Pijpers, J. J. H.; Winkler, M. T.; Surendranath, Y.; Buonassisi, T.; Nocera, D. G. *Proc. Natl. Acad. Sci. U.S.A.* **2011**, *108*, 10056−10061.
(14) Hanna, M. C.; Nozik, A. J. *J. Appl. Phys.* **2006**, *100*, 074510/1−8.
(15) Reece, S. Y.; Hamel, J. A.; Sung, K.; Jarvi, T. D.; Esswein, A. J.; Pijpers, J. J. H.; Nocera, D. G. *Science* **2011**, *334*, 645−648.
(16) Cox, C. R.; Winkler, M. T.; Pijpers, J. J. H.; Buonassisi, T.; Nocera, D. G. *Energy Environ. Sci.* **2013**, *6*, 532−538.
(17) Surendranath, Y.; Bediako, D. K.; Nocera, D. G. *Proc. Natl. Acad. Sci. U.S.A.* **2012**, *109*, 15617−15621.
(18) Surendranath, Y.; Lutterman, D. A.; Liu, Y.; Nocera, D. G. *J. Am. Chem. Soc.* **2012**, *134*, 6326−6336.
(19) Kanan, M. W.; Nocera, D. G. *Science* **2008**, *321*, 1072−1075.
(20) Surendranath, Y.; Dincă, M.; Nocera, D. G. *J. Am. Chem. Soc.* **2009**, *131*, 2615−2620.
(21) Lutterman, D. A.; Surendranath, Y.; Nocera, D. G. *J. Am. Chem. Soc.* **2009**, *131*, 3838−3839.
(22) McAlpin, J. G.; Surendranath, Y.; Dincă, M.; Stich, T. A.; Stoian, S. A.; Casey, W. H.; Nocera, D. G.; Britt, R. D. *J. Am. Chem. Soc.* **2010**, *132*, 6882−6883.
(23) Kanan, M. W.; Yano, J.; Surendranath, Y.; Dincă, M.; Yachandra, V. K.; Nocera, D. G. *J. Am. Chem. Soc.* **2010**, *132*, 13692−13701.
(24) Surendranath, Y.; Kanan, M. W.; Nocera, D. G. *J. Am. Chem. Soc.* **2010**, *132*, 16501−16509.
(25) Dincă, M.; Surendranath, Y.; Nocera, D. G. *Proc. Natl. Acad. Sci. U.S.A.* **2010**, *107*, 10337−10341.
(26) Bediako, D. K.; Lassalle, B.; Surendranath, Y.; Yano, J.; Yachandra, V. K.; Nocera, D. G. *J. Am. Chem. Soc.* **2012**, *134*, 6801−6809.
(27) Steinmiller, E. M. P.; Choi, K.-S. *Proc. Natl. Acad. Sci. U.S.A.* **2009**, *106*, 20633−20636.
(28) Young, E. R.; Costi, R.; Paydavosi, S.; Nocera, D. G.; Bulović, V. *Energy Environ. Sci.* **2011**, *4*, 2058−2061.
(29) Zhong, D. K.; Gamelin, D. R. *J. Am. Chem. Soc.* **2010**, *132*, 4202−4207.
(30) Zhong, D. K.; Cornuz, M.; Sivula, K.; Grätzel, M.; Gamelin, D. R. *Energy Environ. Sci.* **2011**, *4*, 1757−1764.
(31) McDonald, K. J.; Choi, K.-S. *Chem. Mater.* **2011**, *23*, 1686−1693.
(32) Seabold, J. A.; Choi, K.-S. *Chem. Mater.* **2011**, *23*, 1105−1112.
(33) Pilli, S. K.; Furtak, T. E.; Brown, L. D.; Deutsch, T. G.; Turner, J. A.; Herring, A. M. *Energy Environ. Sci.* **2011**, *4*, 5028−5034.
(34) Zhong, D. K.; Choi, S.; Gamelin, D. R. *J. Am. Chem. Soc.* **2011**, *133*, 18370−18377.
(35) Jeon, T. H.; Choi, W.; Park, H. *Phys. Chem. Chem. Phys.* **2011**, *13*, 21392−21401.
(36) Wang, D.; Li, R.; Zhu, J.; Shi, J.; Han, J.; Zong, X.; Li, C. *J. Phys. Chem. C* **2012**, *116*, 5082−5089.
(37) Pilli, S. K.; Deutsch, T. G.; Furtak, T. E.; Turner, J. A.; Brown, L. D.; Herring, A. M. *Phys. Chem. Chem. Phys.* **2012**, *14*, 7032−7039.
(38) Higashi, M.; Domen, K.; Abe, R. *J. Am. Chem. Soc.* **2012**, *134*, 6968−6971.
(39) Bledowski, M.; Wang, L.; Ramakrishnan, A.; Bétard, A.; Khavryuchenko, O. V.; Beranek, R. *ChemPhysChem* **2012**, *13*, 3018−3024.
(40) Trotochaud, L.; Ranney, J. K.; Williams, K. N.; Boettcher, S. W. *J. Am. Chem. Soc.* **2012**, *134*, 17253−17261.
(41) Lee, S. W.; Carlton, C.; Risch, M.; Surendranath, Y.; Chen, S.; Furutsuki, S.; Yamada, A.; Nocera, D. G.; Shao-Horn, Y. *J. Am. Chem. Soc.* **2012**, *134*, 16959−16962.
(42) Gras, J. M.; Pernot, M. In *Proceedings of the Symposium on Electrode Materials and Processes for Energy Conversion and Storage*; McIntyre, J. D. E., Srinivasan, S., Will, F. G., Eds.; The Electrochemical Society: Pennington, NJ, 1977; Vol. *77-6*, pp 425−440.
(43) Conway, B. E.; Bourgault, P. L. *Can. J. Chem.* **1959**, *37*, 292−307.
(44) Lu, P. W.; Srinivasan, S. *J. Electrochem. Soc.* **1978**, *125*, 1416−1422.
(45) Bockris, J. O'M.; Otagawa, T. *J. Phys. Chem.* **1983**, *87*, 2960−2971.
(46) Conway, B. E.; Liu, T. *J. Chem. Soc., Faraday Trans. 1* **1987**, *83*, 1063−1079.
(47) Ferreira, A. C.; Gonzalez, E. R.; Ticianelli, E. A.; Avaca, L. A.; Matvienko, B. *J. Appl. Electrochem.* **1988**, *18*, 894−898.
(48) Raj, I. A.; Trivdei, D. C.; Venkatesan, V. K. *Bull. Electrochem.* **1988**, *4*, 55−59.
(49) Lyons, M. E. G.; Brandon, M. P. *Int. J. Electrochem. Sci.* **2008**, *3*, 1386−1424.
(50) Conway, B. E.; Liu, T. C. *Mater. Chem. Phys.* **1989**, *22*, 163−182.
(51) Nickell, R. A.; Zhu, W. H.; Payne, R. U.; Cahela, D. R.; Tatarchuk, B. J. *J. Power Sources* **2006**, *161*, 1217−1224.
(52) Parsons, R. In *Advances in Electrochemistry and Engineering*; Delahay, P., Tobias, C. W., Eds.; Interscience: New York, 1961; Vol. *1*, pp 29−64.
(53) Gileadi, E. *Electrode Kinetics for Chemists, Chemical Engineers, and Materials Scientists*; Wiley-VCH: New York, 1993; Chapters 13−14.
(54) Corrigan, D. A. *J. Electrochem. Soc.* **1987**, *134*, 377−384.
(55) Gileadi, E. *Electrode Kinetics for Chemists, Chemical Engineers, and Materials Scientists*; Wiley-VCH: New York, 1993; Chapter 24.
(56) Gileadi, E. *Electrode Kinetics for Chemists, Chemical Engineers, and Materials Scientists*; Wiley-VCH: New York, 1993; Chapter 23.
(57) Gileadi, E. *Electrode Kinetics for Chemists, Chemical Engineers, and Materials Scientists*; Wiley-VCH: New York, 1993; Chapter 10.
(58) Bard, A. J.; Faulkner, L. R. *Electrochemical Methods: Fundamentals and Applications*, 2nd ed.; John Wiley and Sons: New York, 2001; pp 340−344.
(59) Gileadi, E. *Electrode Kinetics for Chemists, Chemical Engineers, and Materials Scientists*; Wiley-VCH: New York, 1993; Chapter 14.
(60) MacDonald, J. J.; Conway, B. E. *Proc. R. Soc. London* **1962**, *269*, 419−440.
(61) Damjanovic, A.; Jovanovic, B. *J. Electrochem. Soc.* **1976**, *123*, 374−381.
(62) Lyons, M. E. G.; Brandon, M. P. *Int. J. Electrochem. Sci.* **2008**, *3*, 1425−1462.
(63) Gileadi, E. *Electrode Kinetics for Chemists, Chemical Engineers, and Materials Scientists*; Wiley-VCH: New York, 1993; Chapters 17 and 19.
(64) Goldberg, S.; Criscenti, L. J.; Turner, D. J.; Davis, J. A.; Cantrell, K. J. *Vadose Zone J.* **2007**, *6*, 407−435.
(65) Peak, D.; Luther, G. W.; Sparks, D. L. *Geochem. Cosmochim. Acta* **2003**, *67*, 2551−2560.

(66) Scharifker, B. R.; Habib, M. A.; Carbajal, J. L.; Bockris, J. O'M. *Surf. Sci.* **1986**, *173*, 97−105.
(67) El-Shafei, A. A.; Aramata, A. *J. Solid State Electrochem.* **2007**, *11*, 430−433.
(68) Cotton, F. A.; Wilkinson, G.; Murillo, C.; Bochmann, M. *Advanced Inorganic Chemistry*, 6th ed.; Wiley: New York, 1999; pp 171−173.
(69) Farmer, J. B. In *Advances in Inorganic Chemistry and Radiochemistry*; Emeléus, H. J., Sharpe, A. G., Eds.; Academic Press: New York, 1982; Vol. 25, pp 187−237.
(70) Salentine, C. G. *Inorg. Chem.* **1983**, *22*, 3920−3924.
(71) Risch, M.; Klingan, K.; Heidkamp, J.; Ehrenberg, D.; Chernev, P.; Zaharieva, I.; Dau, H. *Chem. Commun.* **2011**, *47*, 11912−11914.
(72) Choisnet, J.; Evarestov, R. A.; Tupitsyn, I. I.; Veryazov, V. A. *J. Phys. Chem. Solids* **1996**, *57*, 1839−1850.
(73) Koyama, Y.; Kim, Y.-S.; Tanaka, I.; Adachi, H. *Jpn. J. Appl. Phys.* **1999**, *38*, 2024−2027.
(74) Koyama, Y.; Yabuuchi, N.; Tanaka, I.; Adachi, H.; Ohzuku, T. *J. Electrochem. Soc.* **2004**, *151*, A1545−A1551.
(75) McAlpin, J. G.; Stich, T. A.; Ohlin, C. A.; Surendranath, Y.; Nocera, D. G.; Casey, W. H.; Britt, R. D. *J. Am. Chem. Soc.* **2011**, *133*, 15444−15452.
(76) Beverskog, B.; Puigdomenech, I. *Corros. Sci.* **1997**, *39*, 969−980.
(77) Daghetti, A.; Lodi, G.; Trasatti, S. *Mater. Chem. Phys.* **1983**, *8*, 1−90.
(78) Trasatti, S. In *Electrochemistry of Novel Materials*; Lipkowski, J., Ross, P. N., Eds.; VCH: New York, 1994; Chapter 5.
(79) Tewari, P. H.; Campbell, A. B. *J. Colloid Interface Sci.* **1976**, *55*, 531−539.
(80) Faria, L. A.; Prestat, M.; Koenig, J.-F.; Chartier, P.; Trasatti, S. *Electrochim. Acta* **1998**, *44*, 1481−1489.
(81) Wang, L.−P.; Van Voorhis, T. *J. Phys. Chem. Lett.* **2011**, *2*, 2200−2204.
(82) Huynh, M. H. V.; Meyer, T. J. *Chem. Rev.* **2007**, *107*, 5004−5064.
(83) Constentin, C. *Chem. Rev.* **2008**, *108*, 2145−2179.
(84) Reece, S. Y.; Nocera, D. G. *Annu. Rev. Biochem.* **2009**, *78*, 673−699.
(85) Tarasevich, M. R.; Efremov, B. N. In *Electrodes of Conductive Metal Oxides, Part A*; Trasatti, S., Ed.; Elsevier: Amsterdam, 1980; Chapter 5.
(86) Trasatti, S. In *Electrochemistry of Novel Materials*; Lipkowski, J., Ross, P. N., Eds.; VCH: New York, 1994; Chapter 5.
(87) Kinoshita, K. *Electrochemical Oxygen Technology*; Wiley-Interscience: New York, 1992; Chapter 2.
(88) Man, I. C.; Su, H.-Y.; Calle-Vallego, F.; Hansen, H. A.; Martínez, J. I.; Inoglu, N. G.; Kitchin, J.; Jaramillo, T. F.; Nørskov, J. K.; Rossmeisl, J. *ChemCatChem* **2011**, *3*, 1159−1165.
(89) Suntivich, J.; May, K. J.; Gasteiger, H. A.; Goodenough, J. B.; Shao-Horn, Y. *Science* **2011**, *334*, 1383−1385.
(90) Subbaraman, R.; Tripkovic, D.; Chang, K.-C.; Strmcnik, D.; Paulikas, A. P.; Hirunsit, P.; Chan, M.; Greenley, J.; Stamenkovic, V.; Markovic, N. M. *Nat. Mater.* **2012**, *11*, 550−557.